BLOC1S1 control of vacuolar organelle fidelity modulates T_H2 cell immunity and allergy susceptibility.

Rahul Sharma[1], Kaiyuan Wu[2], Kim Han[1], Anna Chiara Russo[1], Pradeep K. Dagur[3], Christian A. Combs[4], Michael N. Sack[1]

[1]Laboratory of Mitochondrial Biology and Metabolism, NHLBI, NIH, Maryland, USA. [2]Cardiovascular Branch, NHLBI, NIH, Maryland, USA. [3]Flow Cytometry Core Facility, NHLBI, NIH, Maryland, USA. [4]Light microscopy Core, NHLBI, NIH, Maryland, USA.

Header: BLOC1S1 and T_H2 immunity

Word Count: Abstract – 222 words, Total word cound 8263. Figures 6, Supplemental Figures 4, Supplemental Tables 4.

Address Correspondence To:
Michael N. Sack (sackm@nih.gov),
Laboratory of Mitochondrial Biology and Metabolism, NHLBI, NIH,
Bldg. 10-CRC, Room 5-3342,
10 Center Drive,
Bethesda, MD 20892, USA

ABSTRACT

The levels of biogenesis of lysosome organelles complex 1 subunit 1 (BLOC1S1) control mitochondrial and endolysosome organelle homeostasis and function. Reduced fidelity of these vacuolar organelles is increasingly being recognized as important in instigating cell-autonomous immune cell activation. We reasoned that exploring the role of BLOC1S1 in $CD4^+$ T cells, may further advance our understanding of regulatory events linked to mitochondrial and/or endolysosomal function in adaptive immunity. Transcript levels of the canonical transcription factors driving $CD4^+$T cell polarization in response to activation showed that, the T_H2 regulator GATA3 and phosphorylated STAT6 were preferentially induced in BLOC1S1 depleted primary $CD4^+$ T (TKO) cells. In parallel, in response to both T cell receptor activation and in response to TH2 polarization the levels of IL-4, IL-5 and IL-13 were markedly induced in the absence of BLOC1S1. At the organelle level, mitochondrial DNA leakage evoked cGAS-STING and NF-kB pathway activation with subsequent T_H2 polarization. The induction of autophagy with rapamycin reduced cytosolic mtDNA and reverses these T_H2 signatures. Furthermore, genetic knockdown of STING and STING and NF-κB inhibition ameliorated this immune regulatory cascade in TKO cells. Finally, at a functional level, TKO mice displayed increased susceptible to allergic conditions including atopic dermatitis and allergic asthma. In conclusion, BLOC1S1 depletion mediated disruption of mitochondrial integrity to initiate a predominant TH2 responsive phenotype via STING-NF-κB driven signaling of the canonical T_H2 regulatory program.

INTRODUCTION

The concept that metabolic remodeling is foundational in controlling immune cell fate, function and polarization is now widely established, and termed immunometabolism (1, 2). Here, metabolic substrates modulate immune cell function, for example by diverting mitochondrial metabolism to preferential biosynthetic functions to support immune cell proliferation (3). At the same accumulation or depletion of specific metabolic substrates function as signaling intermediates to regulate immunity via a multitude of mechanisms including: at the level of immune cell chromatin remodeling (4, 5); by transcriptional (6) or posttranslational regulation (7); via intracellular signal transduction (8); via intracellular organelle effects for example by altering mitochondrial fidelity or autophagy (8); and directly through metabolic remodeling (9). Mitochondria themselves, partially stemming from their prokaryote origins, evoke immune activation following the extrusion of intramitochondrial content into the cytoplasm or extracellular space (3). These mitochondrial components are

termed damage associated molecular patterns (DAMPs), which when recognized by pattern recognition receptors (PRRs), initiate inflammatory signaling (10). The mitochondrial organelle itself, also functions as a signaling platform, where cytosolic PRRs, RIG-I like receptors (RLRs), binds to the mitochondrial associated viral signaling (MAVS) adaptor protein on the outer mitochondrial membrane to amplify antiviral signaling (11). Although less well characterized, immune-modulatory effects may arise from other vacuolar organelles that regulate metabolism, including autophagosomes and the endosome-lysosome system (12-14). We reasoned that the study of intracellular vacuolar organelle regulatory control mechanisms may enhance our understanding of the role of this organelle biology in immune cell activation.

To interrogate this further, we proposed to focus on a candidate protein, BLOC1S1/GCN5L1, which is emerging as an important regulator of mitochondrial and of endo-lysosome homeostasis (15). This pleotropic protein modulates mitochondrial turnover (16, 17) and metabolic function (18, 19), and controls key aspects of autophagosome (17), endosome (20) and lysosome trafficking (21, 22), recycling (23, 24), and function (15, 25, 26). These diverse effects stem from the role of BLOC1S1 as an interacting cofactor that modulates mitochondrial and cytosolic protein acetylation and binds to, and regulates, the function of cytoskeletal and molecular motor proteins. Hence, despite the importance of mitochondrial function in immune modulation and the role of endo-lysosomal biology in antigen presentation, cytokine release and in the control of intracellular pathogens, the role of BLOC1S1 in the immune system has to our knowledge not been previously investigated.

To explore this, conditional knockout *bloc1s1* mice were generated using the CD4-Cre-recombinase, employing a similarly approach to the prior deletion of BLOC1S1 in other cell types including the heart (27) and liver (28). Conditional $CD4^+$ T cell knockout mice (TKO) were viable and showed robust depletion of BLOC1S1 levels. In this paper, we demonstrate that activated TKO $CD4^+$ T_0 cells show significantly higher IL-4, IL-5, and IL-13 production, a greater propensity to T_H2 differentiation and that they had elevated phosphorylation of NF-κB, STAT6 and STING. Moreover, TKO mice were highly susceptible to atopic dermatitis (AD) with a marked eosinophilic infiltrate and produced significantly more type 2 cytokines relative to control animals. In addition, OVA-sensitized TKO mice had significantly increased serum IgE and airway inflammation after OVA challenge. Our data suggest a novel role for BLOC1S1 in controlling $CD4^+$ lineage commitment and type 2 allergic responses.

MATERIALS AND METHODS

Mice.

The NHLBI Animal Care and Use Committee approved all animal studies used in this protocol. The mice were maintained on a 12-h light/dark cycle and housed 3-5 mice per cage with free access to water and normal chow diet (LabDiet, 5001). BLOC1S1 $CD4^+$ T cell knockout (TKO) mice were generated by crossing BLOC1S1$^{flox/flox}$ mice with CD4-Cre-recombinase mice, as we had previously. All mice were generated in the C56BL/6b background. All experiments used 8-12 week old C57BL/6$^{flox/flox}$ (control) and $CD4^+$ TKO mice (backcrossed > 10 generations).

Mouse $CD4^+$ T cell isolation and cytokine assay.

All in vitro assays were performed using between three and five mice per group. $CD4^+$ T cells were negatively selected from the spleenocytes using $CD4^+$ T cell isolation kit (Miltenyi Biotec) and cultured in RPMI 1640 media supplemented with 25 mM HEPES, 10% FBS, and Penicillin/Streptomycin. Mice $CD4^+$ T cells ($4x10^5$/well in 96-well plate) were activated with plate-coated αCD3 (5 µg/ml, Biolegend) and αCD28 (10 µg/ml, Biolegend) for 3 days. Also, $CD4^+$ T cells ($4X10^5$/well in 96-well plate) were differentiated into TH2 T cell subtype by incubation with specific supplement for T_H2 differentiation (mouse IL-2, mouse IL-4 and rat anti mouse IFNγ with 1:100 dilution (STEMCELL Technologies)) and incubated for 3 days on plates coated with aCD3 and aCD28 antibodies. Supernatants were collected, centrifuged to remove cells and debris, and stored at -80^0 C. The levels of cytokines, including IFNγ, TNFα, IL-4, IL-5, IL-13, IL-10, and IL-17 were measured by ELISA (R&D systems). Results were normalized to cell number using CyQuant cell proliferation assay (Invitrogen) or BCA protein assay (Pierce).

Human $CD4^+$ T cell isolation and cytokine assay.

Primary peripheral blood mononuclear cells (PBMCs) were isolated from human blood by density centrifugation using Lymphocyte Separation Medium (MP Biomedicals). CD4+ T cells were negatively selected from PBMCs using $CD4^+$ T cell isolation kit (Miltenyi Biotec) and cultured in RPMI 1640 media supplemented with 25 mM HEPES, 10% FBS, and Penicillin/Streptomycin. Human $CD4^+$ T cells ($4X10^5$/well in 96-well plate) were activated with plate-coated αCD3 (5µg/ml, Biolegend) and αCD28 (10µg/ml, Biolegend) for 3 days. Supernatants were collected, centrifuged to remove cells and debris, and stored at -80^0 C. The levels of cytokines, including IL-4, IL-5 and IL-13 were measured by ELISA (R&D systems). Results were normalized to cell number using CyQuant cell proliferation assay (Invitrogen) or BCA protein assay (Pierce).

RNA Isolation and Quantitative PCR (qRT-PCR) analysis.

Total RNA was extracted using NucleoSpin RNA kit (Macherey-Nagel) and cDNA was synthesized with the SuperScript III First-Strand Synthesis System for RT-PCR (Thermo Fischer Scientific). Quantitative real-time PCR was performed using FastStart Universal SYBR Green master (Roche) and run on LightCycler 96 Systems (Roche). Relative gene expression was quantified by normalizing cycle threshold values with 18S rRNA using the $2^{-\Delta\Delta Ct}$ cycle threshold method. To measure mitochondrial DNA (mtDNA) in the cytosol of $CD4^+$ T cells, 8 × 10^6 cells were homogenized with a Dounce homogenizer in 10 mM Tris solution (pH 7.4), containing 0.25 M sucrose, 25 mM KCl, 5 mM $MgCl_2$ and protease inhibitor, and then centrifuged at 700 × g for 10 min at 4°C. Cytosolic fractions were prepared by centrifugation at 10,000 × g for 30 min at 4°C and DNA was isolated from them using the DNeasy Blood & Tissue kit (Qiagen). The copy number of mitochondrial DNA encoding 16S RNA (RNR2) and non-coding D-loop region was measured by quantitative real-time qRT-PCR. Primer sequences are provided in Supplementary Table 1.

Immunoblot Analysis.

Mice or Human CD4 T cells were lysed using RIPA buffer supplemented with protease inhibitor cocktail (Roche) and phosphatase inhibitors (Pierce). Lysates were separated by NuPAGE 4-12 % Bis-Tris Gels (Thermo Fischer Scientific) and transferred to nitrocellulose membranes (Trans-Blot Turbo Transfer Systems (Bio-Rad Laboratories). Membranes were blocked with Odyssey Blocking Buffer (Li-Cor) and incubated with appropriate antibodies overnight at 4^0 C. List of Primary antibodies used are provided in Supplementary Table 2. The secondary antibody conjugated with IRDye 800 CW or IRDye 680RD (Li-Cor) were then incubated for 1 hour at room temperature. Immunoblots were scanned using an Odyssey Clx imaging system (Li-Cor Biosciences). Protein band intensity was quantified using ImageJ software (National institute of health).

Flow cytometry for cell phenotyping.

Activated TKO $CD4^+$ T cells were activated with Cell stimulation cocktail plus protein transport inhibitors (eBioscience) and PMA (500 ng/ml, Sigma) for 4 hrs and then incubated with antibodies targeting cell surface markers, transcription factors and (BD, Biolegend). Data were acquired with FACSymphony (BD) and post-acquisition analysis was performed using Flowjo 9.9.6 (Treestar Inc.). Analysis excluded debris and doublets using light scatter measurements, and dead cells by live/dead stain. Gating strategies used to identify immune cell subsets are provided in Supplementary Table 3. Briefly, the cells were first gated for singlets (FSC-H *vs*. FSC-A) and further analyzed for their uptake of the Live/Dead Zombi violet stain (Biolegend)

to determine live versus dead cells in $CD3^+CD4^+$. The expression of transcription factors and cytokines is then determined for T cell polarization within this gated population.

Characterization of BLOC1S1 signaling in primary human T cells

Primary $CD4^+$ T cells were cultured in RPMI with 1% FBS on αCD3/αCD28 antibody-coated plates for 3 days. The following inhibitors were added to the cells for 24 hours before harvesting: the NF-κB inhibitor JSH23 (2 μM, Tocris Bioscience), STING inhibitor H151 (5 μM, Tocris Bioscience), or Rapamycin (2 μM, Selleckchem). Cytotoxicity was assessed using the CyQUANT LDH Cytotoxicity Assay (Invitrogen). On the third day, cells were centrifuged for Western blot or RNA analysis and the supernatant was collected for ELISA assay.

Genetic knockdown experiments.

For the siRNA knockdown experiments, primary $CD4^+$ T cells were transfected with 1.5 μM SMARTpool Accell BLOC1Sa and STING siRNA or Accell control siRNA in Accell siRNA delivery medium (Dharmacon). Knockdown cells were activated on αCD3/αCD28 (Biolegend) antibody-coated plates for 3 days.

Experimental atopic dermatitis.

Calcipotriol (MC903:Sigma Aldrich) was resuspended in ethanol at 50 μM. A total of 1 nM was applied daily to the outer and inner surfaces of the left ear (20 ml/ear) as described previously (29) for 15 days, as follow: 5 days topical treatment, 2 days interruption, 5 days treatment, 2 days interruption, 1 day topical treatment. Ethanol (20 ml/ear) was applied to the contralateral ear as the vehicle control. Auricular lymph node of the MC903 or vehicle-treated mice were extracted at the end of the study and ear sections were either fixed in 10% Formalin for histology or stored at -80^0 C. $CD4^+$ T cells were negatively selected from the minced auricular lymph nodes using the $CD4^+$ T cell isolation kit (Miltenyi Biotec) and cultured in RPMI 1640 media supplemented with 25 mM HEPES, 10% FBS, and Penicillin/Streptomycin. Auricular lymph node $CD4^+$ T cells ($2x10^5$/well in 96-well plate) were activated with plate-coated αCD3 and αCD28 for 3 days. Supernatants were collected, centrifuged to remove cells and debris, and stored at -80 ^{0}C.

Experimental allergic airway inflammation.

Mice were sensitized with ovalbumin (OVA, MedChem Express) to induce allergic airway inflammation (30). Mice were administered 20 mg OVA in 4mg alum hydroxide (InvivoGen) by intraperitoneal (i.p) injection on days 0 and 7 and subjected to airway exposure with 40μg OVA in PBS on day 11-14. 24 h after the last OVA aerosol challenge, lungs from allergen sensitized and challenged mice were taken and a section was fixed in 4% paraformaldehyde (PFA) for

histology and the residual lung was used to isolate $CD4^+$ T cells. List of reagents provided in supplementary table 4.

Histology.

Lungs from the allergen-sensitized and challenged mice experiment and ears from the MC903 and ethanol vehicle treated mice experiment were fixed in 4% PFA for histology. The fixed samples were processed and stained with hematoxylin and eosin (H&E) and Ki67 immunohistochemical staining (Histoserv).

Immunofluorescence staining and microscopy.

CD4+ T cells were activated as earlier described and adhered to glass slides coated with poly-L-lysine (Sigma Aldrich). The cells were fixed with 4% paraformaldehyde for 15 min at room temperature. After the cells were washed three times with PBS, cells were blocked in 5% BSA and 0.1% Triton X for 1 hour at room temperature. Cells were then incubated with appropriate primary antibody overnight at 4^0C. Then, the cells were washed three times with PBS and were incubated with the appropriate Alexa secondary Abs for 60 minute at room temperature in the dark. Nuclei were counterstained blue with DAPI. All fluorescent imaging performed using a Zeiss 880 confocal microscope and a Plan-Apochromat 63x(1.4 N.A.). Four color images of DAPI, Alexa 488, Alexa 561, and Alexa 633 were collected using 405nm, 488nm, 561nm and 633nm with emission bandwidths of 415-480nm, 490-556nm, 565-659nm and 641-735nm respectively. Three color imaging of DAPI, Alexa 488, and Alexa 561 were collected using 405nm, 488nm, and 561nm excitation with 415-481nm, 480-569nm, and 570-709nm, respectively. Pixels sizes varied from 0.68-0.98 microns. The pinhole was set to 1A.U. for all experiments and z-stacks were taken with an interslice spacing of 300nm. For experiments where intensity was compared between treatments laser excitation power did not vary more than 0.1%. Images were deconvolved assuming an idealized point spread function using the Hyugens software program (SVI, Hilversum, Netherlands)..

Quantification of confocal Immunofluorescent images

Immunofluorescent images were quantified using the open-source program FIJI (31). In short, regions of interest (ROI's) were manually drawn on each cell to segment the nucleus from the cytoplasm. From the segmented images summed intensity from each compartment across z-stacks was then calculated.

Statistical analysis.

Graphs were plotted and analyzed using GraphPad Prism 9. Statistical analysis was performed with either a two-tailed unpaired student t test (for paired data) or two-way ANOVA with Tukey's post hoc test for experiments with multiple groups. Probability values of <0.05 were considered statistically significant. Data are shown as mean ± SEM. Asterisks denote p value (*p<0.05, **p<0.01, ***p<0.001 and ****p<0.0001).

RESULTS

BLOC1S1 depleted CD4$^+$ T cell preferentially augments T_H2 immune cell responsiveness.

The approach to generate CD4$^+$ T cell-specific BLOC1S1 knockout (TKO) mice is depicted in Supplemental Figure 1A. Separation of CD4$^+$ cells from the residual splenic pool (CD4- cells) as depicted in Supplemental Figure 1B, with subsequent qRT-PCR shows robust reduction in bloc1s1 transcript levels in the CD4$^+$ pool compared to the Lox-P littermate control mice (Supplemental Figure 1C). To initially characterize CD4$^+$ T cell immunoresponsiveness, primary CD4$^+$ T cells were activated by antibodies directed against CD3 and CD28 to engage the T cells receptors (TCRs). ELISA assays to assess cytokine secretion showed that TCR engagement in TKO cells significantly increased levels of interleukins (ILs) 4, 5, 10 and 13, reduced IL-17 and without effects on interferon gamma (IFN-γ) and TNFα compared to control cells (Figure 1A). We then assayed the transcript levels of canonical transcription factors driving CD4$^+$ T cell polarization in response to TCR activation. The expression of *tbet* (Tbx21 - T_H1 polarizing transcription factor (TF)), *rorc* (RAR related orphan receptor C – Th17 polarizing TF) and *foxp3* (forkhead TF family member p3 – Treg polarizing TF) were not different between genotypes in T_H0 cells (Supplemental Figure 1D). In contrast, the gene encoding GATA3, and its cognate protein level were markedly induced in TKO cells (Figure 1B-D). Flow cytometry analysis validated the increase in GATA3$^+$,IL4$^+$ in TKO CD4$^+$ T cells (Figure 1E) with no changes in TBET$^+$,IFNg+ or Rorc$^+$,IL17$^+$ cells (Supplemantal Figure 1E). The gating profiles of CD4$^+$ T cells for flow cytometry is shown in Supplemental Figure 1F. We then assessed the effect T_H2 polarization on the secretion of canonical T_H2 cytokines. Consistent with the T_H0 data, levels of IL-4, IL-5 and IL-13 secretion were induced to a greater extent in the TKO cells (Figure 1F). To further validate this response to diminished BLOC1S1 levels siRNA targeting bloc1s1 or scrambled constructs were transfected into primary human CD4$^+$ T cells. The efficiency of Bloc1s1 knockdown (KD) was ≈ 80% and transcript levels of GATA3 were induced coordinately (Supplemental Figure 1G). In parallel, transcript levels and secreted T_H2 cytokines were induced to a greater extent following bloc1s1 knockdown (Supplemental Figures G-H). As GATA3 functions as the master regulator driving T_H2

differentiation and given the effect of reduced BLOC1S1 on T_H2 cytokine release, this manuscript subsequently focused on the study of BLOC1S1 effects on T_H2 biology.

Enhanced phosphorylation of IKK, NF-κB and STAT6 and GATA3 protein levels in TKO CD4$^+$ T cells

The transcriptional and signaling pathways underpinning T_H2 lineage polarization are well characterized, with GATA3 and STAT6 playing central roles (32). More recently in the context of allergic asthma, NF-κB signaling has been implicated in GATA3 induction and subsequent T_H2 polarization (30). We therefore explored the activity of these regulatory molecules. To investigate these pathways splenic CD4$^+$ T cells were isolated from control and TKO mice and exposed to TCR engagement. In activated T_H0 cells, in the absence of BLOC1S1, phosphorylation and activation of IκB, NF-κB and STAT6 were markedly induced, in parallel with the induction of GATA3 (Figure 2A-B). In support of the functional contribution of this NF-κB - GATA3 pathway, pharmacological inhibition of NF-κB with JSH23 resulted in diminished NF-κB phosphorylation and GATA3 steady-state levels relative to DMSO treated controls (Figure 2C-D). In parallel, JSH23 blunted T_H2 cytokine induction to a greater extent in the TKO T_H0 cells (Figure 2E).

Vacuolar organelle perturbations drive BLOC1S1 accentuated T_H2 immunity via STING induction.

Interestingly, nucleic acid sensing has been established to drive T_H2 rather than T_H1 or T_H17 differentiation (33) and mitochondrial DNA (mtDNA) release activates the double-stranded nucleic acid sensing cGAS-STING PRR pathway (34). Considering the role of BLOC1S1 in sustaining mitochondrial fidelity (15), we investigated this as a putative mechanism whereby BLOC1S1 depletion regulates T_H2 signaling. The amount of cytosolic mtDNA, as measured using qRT-PCR showed higher levels of the mitochondrial encoded 16S RNA (RNR2) and non-coding D-loop region of mtDNA in the cytosol in TKO cells (Figure 3A). Given this, it was unsurprisingly that the levels of cGAS and extent of STING phosphorylation, as measured by immunoblot analysis, were induced in TKO CD4$^+$ T cells (Figure 3B-C). To validate this, confocal microscopy using fixed CD4$^+$ T cells were labelled with fluorescent-tagged antibodies to endogenous STING in parallel with nuclear DNA labeling with DAPI. Here too, STING levels were confirmed to be elevated in the TKO cells (Figure 3D-E). In parallel, fluorescent-tagged antibodies targeting cGAS and cytosolic dsDNA (35), similalry showed their induction and greater cytosolic colocalization in TKO cells (Figure 3F-G). As BLOC1S1 deficiency is known

to result in autophagosome accumulation (24) and evident here by increased LAMP1 and LC3-II in TKO cells (Figure 3B-C and Supplemental Figure 2), we assessed if driving autophagy with rapamycin may ameliorate this inflammatory program. Here the inhibition of mTORC1 with rapamycin blunted LAMP1 levels in parallel with a further increase in LC3-II levels in TKO cells, suggesting induction of autophagy (Figure 3H-I). In parallel, rapamycin reduced cytosolic levels of mtDNA in control and TKO cells (Figure 3J) and blunted IL-4, IL-5 and IL-13 secretion to a greater extent in the TKO cells (Figure 3K).

STING activation orchestrates NF-kB activation to drive T_H2 activation.

To functionally validate that cGAS-STING activation, contributed towards NF-κB signaling and T_H2 activation, STING was inhibited using H151 (36) or depleted via STING siRNA. H151 supplementation of primary T_H0 $CD4^+$ T cells, reduced STING levels in TKO cells (Figure 4A-B). Furthermore, the activation of IκBα, NF-κB and STAT6 were all more robustly attenuated in the TKO cells (Figure 4A-B). GATA3 levels were blunted in parallel (Figure 4A-B). Consistently, the secretion of IL-4, IL-5 and IL-13 were blunted in the TKO cells in the presence of H151 (Figure 4C). Interestingly, H151 blunted IFN-γ to a similar extent in control and TKO cells (Supplemental Figure 3A). STING knockdown (KD) was highly effective in both lineages (Supplemental Figure 3B). As STING levels were more pronounced in TKO cells, the effect of STING KD was also more robust in these $CD4^+$ T cells. Here we see robust reductions STING levels, and in IκBα and NF-κB activation (Figure 4D-E). In parallel, STING KD reduced GATA3 expression to a greater extent in the TKO $CD4^+$ T cells (Figure 4D-E). Similarly, STING KD signficiantly blunted IL-4, IL-5 and IL-13 secretion in the TKO cells, with a modest reduction in IL-13 secretion in control cells (Figure 4F). Similarly, and consistent with H151 supplementation, STING KD blunted IFN-γ to similar extents in control and TKO cells (Supplemental Figure 3C). The proposed mitochondrial fidelity pathway following BLOC1S1 depletion in T_H2 cells is schematized in Figure 4G.

TKO mice are more susceptible to T_H2-linked allergic disease models.

As atopic disorders are driven by an elevated T_H2 response we exploited different atopy models to functionally validate the susceptibility of T_H2 polarization in the absence of BLOC1S1. The first model explored was atopic dermatitis (AD) induced by the topical exposure to the ear pinnae of the vitamin D3 analogue Calcipotriol (MC903) (29). The protocol is schematized in Figure 5A. This response to MC903 appeared similar in both sexes (Supplemental Figure 4A). Although, topical application of MC903 vs. ethanol control triggered an AD response with increased skin thickness in all mice, TKO mice exhibited an earlier lesion onset with more severe disease (Figure 5B). Histological examination of the red scaly lesioned skin showed greater epidermal hyperplasia with dermal lymphocyte infiltration in the TKO mice

(Figure 5C and Supplemental Figure 4B). In parallel, the marker of cell proliferation, Ki67 was markedly induced in the TKO mice (Figure 5D). Consistent with atopy, TKO mice showed higher plasma levels of IgE under basal conditions, with a further exaggeration in response to the topical application of MC903 (Figure 5E). Interestingly, although BLOC1S1 deficiency was restricted to $CD4^+$ T cells, qRT-PCR of whole skin samples showed that transcripts encoding bloc1s1 were blunted in this MC903 AD model in both the control and TKO mice (Figure 5F). Finally, in this model, the quantification of cytokine secretion from $CD4^+$ T cells extracted from the auricular Lymph nodes showed enhanced IL-4, IL-5, and IL-13 levels in response to topical MC903 treatment in the TKO mice (Figure 5G-H).

We then exposed control and TKO mice to OVA-induced allergic airway inflammation as a second atopic model (30, 37). Mice were OVA challenged both systematically and via aerosol to evoke airway inflammation as depicted in Figure 6A. Histological analysis of lungs of OVA sensitized mice showed more marked peribronchial inflammation with infiltrating eosinophil infiltration in the TKO mice (Figure 6B). Consistent with a greater allergen specific type 2 response, OVA TKO mice similarly showed plasma IgE levels (Figure 6C). The TKO mice also showed greater production of IL-4 and IL-13 in $CD4^+$ T cells extracted from the lungs of OVA exposed mice (Figure 6D). Furthermore, the response to OVA was relatively more robust in the TKO mice versus control mice (Figure 6E). Interestingly, and consistent with the findings in primary $CD4^+$ T cell in-vitro studies, transcripts encoding STING were induced in ear from the AD model and in whole lung tissue from the allergic asthma model (Supplemental Figure 4C).

Discussion

In this study we find that the absence of BLOC1S1 in $CD4^+$ T cells, results in the preferential polarization into the T_H2 cell lineage in response to TCR engagement. This programing appears to be driven by perturbed mitochondrial fidelity possibly coupled to incomplete autophagic clearance of mtDNA. The persistently increased cytosolic mtDNA, activates the cGAS-STING immune surveillance program. Downstream of this, NF-κB activation is linked with the induction of GATA3 and phosphorylated STAT6 to amplify T_H2 lineage responsiveness. Consistent with this immune phenotype, the BLOC1S1 TKO mice show greater susceptibility to allergic conditions including atopic dermatitis and allergic asthma.

The cell autonomous program promoting TH2 polarization is well established with respect to the role of GATA3 and STAT6 signaling. However, the roles of mtDNA initiated signaling and cGAS-STING activation has not been well established in adaptive immune cells. In contrast,

in innate immunity, mtDNA functions as a canonical damage associated molecular pattern (DAMP) to initiate cGAS-STING signaling myeloid cells (34), and to drive neutrophil NETosis (38). Recent data does show that aging is linked with the disruption of lysosome proteasomal function with a concomitant increase in mtDNA and inflammaging in human $CD4^+$ T cells (39). Although, the role of cGAS-STING or NF-κB was not assessed in that study (39). Conversely, in the murine tumor microenvironment $CD4^+$ T-intrinsic STING activation drives T_H1 and T_H9 activation (40). Interestingly here, the T_H1, but not the T_H9 phenotype was dependent on type 1 interferon signaling, although both lineages were dependent on MTOR and NF-κB activity (40). At the same time, the genetic disruption of NF-κB signaling attenuated allergic airway induced T_H2 polarization (30). Together these data highlight that the fate of distinct $CD4^+$ T cell subsets have different signaling pathways, that may be moderated in part by the in-situ environment and immune cell cross talk. Our study adds to these finding by showing the depleting BLOC1S1 initiates a mtDNA, cGAS-STING and NF-κB integrated pathway that preferentially augments T_H2 cell responsiveness and susceptibility to atopy.

In innate immunity, TBK1 is a canonical kinase in the STING mediated induction of NF-kB too enable signal transduction (41). This STING mediated activation of TBK1 results in the subsequent phosphorylation of NF-κB essential modulator (NEMO), a regulatory subunit of the IKK (inhibitor of NF-κB kinase) complex (42). Phosphorylated NEMO then activates the IKK complex, leading to the degradation of inhibitory IkB proteins and the release and nuclear translocation of active NF-κB (42). In parallel, TBK1 activation promotes degradation of STING via the induction of autophagy as a negative regulatory feedback loop (43). Interestingly, the absence of BLOC1S1 is known to constipate the autophagolysosomal degradation pathway (24), and whether this pathway is operational in augmented cytosolic mtDNA and or accumulation of STING in the TKO cells warrants further evaluation. Contrary to the effects on innate immunity, the conditional knockout of TBK1 in $CD4^+$ T cells resulted in the induction of IFN-γ and of $CD4^+$ memory cells, and the pharmacologic inhibition of TBK1 blunted experimental autoimmune encephalitis (44). Conversely our study shows the TKO mice exhibit an increased T_H2 profile with the exacerbation of allergic disease in parallel with increased TBK1 phosphorylation. Although these data remain to be reconciled, this may point to the specific roles of BLOC1S1 in mitochondrial quality control and/or in autophagosome homeostatic functions to alleviate cytosolic DAMPS and thereby reduce T_H2 polarization.

The concept that intracellular quality control programs moderate immune responsiveness is well established in programs controlling autophagy and mitochondria homeostasis. Emerging studies are implicating immunoregulatory effects of programs controlling lipid handling and endo-lysosomal function. At a reductionist levels, these distinct programs are being well

characterized, and at a systemic biology perspective, these programs play integrated roles. Interestingly, BLOC1S1 as a nutrient-sensing homeostatic mediator contribute towards the control of all these programs (15, 25). In this manuscript, we show that the absence of BLOC1S1 has a preferential effect on enhancing T_H2 immune cell responsiveness. The comprehensive mechanisms of action remain to be determined. However, our initial findings support both that the extrusion of mtDNA from mitochondria and the accumulation of STING on endo-lysosomes which together may amplify both canonical and non-canonical T_H2-linked immune responsiveness.

Genetic defects in BLOC1S1 have been associated with juvenile leukodystrophy (45) and has recently been linked with a reduction in lysosome content and increased lipid stores (26). Although juvenile leukodystrophy is associated with neuroinflammation, a direct link to T_H2 biology does not appear to have been explored (46). Furthermore, lipid biology is emerging as a mediator pathway in $CD4^+$ T cell polarization (47). At the same time, it is interesting that transcriptomic analysis in 16 atopic dermatitis subjects, shows that BLOC1S1 expression is significantly blunted in association with this allergic ichthyosis (48). Given that human iPSC's are available that incorporate BLOC1S1 mutations (49), these cells have the potential for the direct exploration of the role of BLOC1S1 genetic mutations in $CD4^+$ T cell biology.

In conclusion, we show that in the absence of BLOCS1, which exhibits perturbed mitochondrial and endolysosomal functioning, that $CD4^+$ T cells are preferentially polarization towards the TH2 lineage. This is shown to be mediated in part, but cytosolic mtDNA accumulation, STING activation with downstream NFkB signaling, which drives the canonical GATA3 and STAT6 signaling to augment T_H2 responsiveness. This T_H2 signature is validated in vivo with increased atopic dermatitis and allergic asthma in the BLOC1S1 knockout mice. This model should allow us to further dissect out the integrated roles of mitochondrial and endolysosomal homeostasis programs in driving $CD4^+$ T cell fates.

Acknowledgements

This research was supported by the NHLBI Division of Intramural Research (MNS – ZIA-HL005199). We thank and acknowledge the assistance of the NHLBI Laboratory Animal Core Facility. Finally, we thank Nina Boehm (née Klimova) Ph.D., who initiated this project in the laboratory.

References

1. Makowski, L., M. Chaib, and J. C. Rathmell. 2020. Immunometabolism: From basic mechanisms to translation. *Immunol Rev* 295: 5-14.
2. Ryan, D. G., and L. A. J. O'Neill. 2020. Krebs Cycle Reborn in Macrophage Immunometabolism. *Annu Rev Immunol* 38: 289-313.
3. Sack, M. N. 2018. Mitochondrial fidelity and metabolic agility control immune cell fate and function. *J Clin Invest* 128: 3651-3661.
4. Roy, D. G., J. Chen, V. Mamane, E. H. Ma, B. M. Muhire, R. D. Sheldon, T. Shorstova, R. Koning, R. M. Johnson, E. Esaulova, K. S. Williams, S. Hayes, M. Steadman, B. Samborska, A. Swain, A. Daigneault, V. Chubukov, T. P. Roddy, W. Foulkes, J. A. Pospisilik, M. C. Bourgeois-Daigneault, M. N. Artyomov, M. Witcher, C. M. Krawczyk, C. Larochelle, and R. G. Jones. 2020. Methionine Metabolism Shapes T Helper Cell Responses through Regulation of Epigenetic Reprogramming. *Cell Metab* 31: 250-266 e259.
5. Chen, X., Y. Lu, Z. Zhang, J. Wang, H. Yang, and G. Liu. 2015. Intercellular interplay between Sirt1 signalling and cell metabolism in immune cell biology. *Immunology* 145: 455-467.
6. Han, K., K. Singh, M. J. Rodman, S. Hassanzadeh, K. Wu, A. Nguyen, R. D. Huffstutler, F. Seifuddin, P. K. Dagur, A. Saxena, J. P. McCoy, J. Chen, A. Biancotto, K. E. R. Stagliano, H. L. Teague, N. N. Mehta, M. Pirooznia, and M. N. Sack. 2021. Fasting-induced FOXO4 blunts human CD4(+) T helper cell responsiveness. *Nat Metab* 3: 318-326.
7. Traba, J., M. Kwarteng-Siaw, T. C. Okoli, J. Li, R. D. Huffstutler, A. Bray, M. A. Waclawiw, K. Han, M. Pelletier, A. A. Sauve, R. M. Siegel, and M. N. Sack. 2015. Fasting and refeeding differentially regulate NLRP3 inflammasome activation in human subjects. *J Clin Invest* 125: 4592-4600.
8. Palma, C., C. La Rocca, V. Gigantino, G. Aquino, G. Piccaro, D. Di Silvestre, F. Brambilla, R. Rossi, F. Bonacina, M. T. Lepore, M. Audano, N. Mitro, G. Botti, S. Bruzzaniti, C. Fusco, C. Procaccini, V. De Rosa, M. Galgani, C. Alviggi, A. Puca, F. Grassi, T. Rezzonico-Jost, G. D. Norata, P. Mauri, M. G. Netea, P. de Candia, and G. Matarese. 2021. Caloric Restriction Promotes Immunometabolic Reprogramming Leading to Protection from Tuberculosis. *Cell Metab* 33: 300-318 e312.
9. Wagner, A., C. Wang, J. Fessler, D. DeTomaso, J. Avila-Pacheco, J. Kaminski, S. Zaghouani, E. Christian, P. Thakore, B. Schellhaass, E. Akama-Garren, K. Pierce, V. Singh, N. Ron-Harel, V. P. Douglas, L. Bod, A. Schnell, D. Puleston, R. A. Sobel, M. Haigis, E. L. Pearce, M. Soleimani, C. Clish, A. Regev, V. K. Kuchroo, and N. Yosef. 2021. Metabolic modeling of single Th17 cells reveals regulators of autoimmunity. *Cell* 184: 4168-4185 e4121.
10. Kemper, C., and M. N. Sack. 2022. Linking nutrient sensing, mitochondrial function, and PRR immune cell signaling in liver disease. *Trends Immunol* 43: 886-900.
11. Belgnaoui, S. M., S. Paz, and J. Hiscott. 2011. Orchestrating the interferon antiviral response through the mitochondrial antiviral signaling (MAVS) adapter. *Curr Opin Immunol* 23: 564-572.
12. Menon, D., A. Bhapkar, B. Manchandia, G. Charak, S. Rathore, R. M. Jha, A. Nahak, M. Mondal, M. Omrane, A. K. Bhaskar, L. Thukral, A. R. Thiam, and S. Gandotra. 2023. ARL8B mediates lipid droplet contact and delivery to lysosomes for lipid remobilization. *Cell Rep* 42: 113203.
13. Yin, H., H. Wu, Y. Chen, J. Zhang, M. Zheng, G. Chen, L. Li, and Q. Lu. 2018. The Therapeutic and Pathogenic Role of Autophagy in Autoimmune Diseases. *Front Immunol* 9: 1512.
14. Baixauli, F., R. Acin-Perez, C. Villarroya-Beltri, C. Mazzeo, N. Nunez-Andrade, E. Gabande-Rodriguez, M. D. Ledesma, A. Blazquez, M. A. Martin, J. M. Falcon-Perez, J. M. Redondo, J. A. Enriquez, and M. Mittelbrunn. 2015. Mitochondrial Respiration Controls Lysosomal Function during Inflammatory T Cell Responses. *Cell Metab* 22: 485-498.
15. Wu, K., I. Scott, L. Wang, D. Thapa, and M. N. Sack. 2021. The emerging roles of GCN5L1 in mitochondrial and vacuolar organelle biology. *Biochim Biophys Acta Gene Regul Mech* 1864: 194598.

16. Scott, I., B. R. Webster, C. K. Chan, J. U. Okonkwo, K. Han, and M. N. Sack. 2014. GCN5-like protein 1 (GCN5L1) controls mitochondrial content through coordinated regulation of mitochondrial biogenesis and mitophagy. *J Biol Chem* 289: 2864-2872.
17. Webster, B. R., I. Scott, K. Han, J. H. Li, Z. Lu, M. V. Stevens, D. Malide, Y. Chen, L. Samsel, P. S. Connelly, M. P. Daniels, J. P. McCoy, Jr., C. A. Combs, M. Gucek, and M. N. Sack. 2013. Restricted mitochondrial protein acetylation initiates mitochondrial autophagy. *J Cell Sci* 126: 4843-4849.
18. Thapa, D., K. Wu, M. W. Stoner, B. Xie, M. Zhang, J. R. Manning, Z. Lu, J. H. Li, Y. Chen, M. Gucek, M. P. Playford, N. N. Mehta, D. Harmon, R. M. O'Doherty, M. J. Jurczak, M. N. Sack, and I. Scott. 2018. The protein acetylase GCN5L1 modulates hepatic fatty acid oxidation activity via acetylation of the mitochondrial beta-oxidation enzyme HADHA. *J Biol Chem* 293: 17676-17684.
19. Wang, L., L. Zhu, K. Wu, Y. Chen, D. Y. Lee, M. Gucek, and M. N. Sack. 2020. Mitochondrial General Control of Amino Acid Synthesis 5 Like 1 Regulates Glutaminolysis, Mammalian Target of Rapamycin Complex 1 Activity, and Murine Liver Regeneration. *Hepatology* 71: 643-657.
20. Zhang, A., X. He, L. Zhang, L. Yang, P. Woodman, and W. Li. 2014. Biogenesis of lysosome-related organelles complex-1 subunit 1 (BLOS1) interacts with sorting nexin 2 and the endosomal sorting complex required for transport-I (ESCRT-I) component TSG101 to mediate the sorting of epidermal growth factor receptor into endosomal compartments. *J Biol Chem* 289: 29180-29194.
21. Pu, J., C. Schindler, R. Jia, M. Jarnik, P. Backlund, and J. S. Bonifacino. 2015. BORC, a multisubunit complex that regulates lysosome positioning. *Dev Cell* 33: 176-188.
22. Wu, K., L. Wang, Y. Chen, M. Pirooznia, K. Singh, S. Walde, R. H. Kehlenbach, I. Scott, M. Gucek, and M. N. Sack. 2018. GCN5L1 interacts with alphaTAT1 and RanBP2 to regulate hepatic alpha-tubulin acetylation and lysosome trafficking. *J Cell Sci* 131: pii: jcs221036.
23. John Peter, A. T., J. Lachmann, M. Rana, M. Bunge, M. Cabrera, and C. Ungermann. 2013. The BLOC-1 complex promotes endosomal maturation by recruiting the Rab5 GTPase-activating protein Msb3. *J Cell Biol* 201: 97-111.
24. Wu, K., A. Seylani, J. Wu, X. Wu, C. K. E. Bleck, and M. N. Sack. 2021. BLOC1S1/GCN5L1/BORCS1 is a critical mediator for the initiation of autolysosomal tubulation. *Autophagy* 17: 3707-3724.
25. Scott, I., L. Wang, K. Wu, D. Thapa, and M. N. Sack. 2018. GCN5L1/BLOS1 Links Acetylation, Organelle Remodeling, and Metabolism. *Trends Cell Biol* 28: 346-355.
26. Wu, K., J. Zou, and M. N. Sack. 2023. The endo-lysosomal regulatory protein BLOC1S1 modulates hepatic lysosomal content and lysosomal lipolysis. *Biochem Biophys Res Commun* 642: 1-10.
27. Thapa, D., M. Zhang, J. R. Manning, D. Guimaraes, M. Stoner, R. M. O'Doherty, S. Shiva, and I. Scott. 2017. Acetylation of mitochondrial proteins by GCN5L1 promotes enhanced fatty acid oxidation in the heart. *Am J Physiol Heart Circ Physiol*: ajpheart 00752 02016.
28. Wang, L., I. Scott, L. Zhu, K. Wu, K. Han, Y. Chen, M. Gucek, and M. N. Sack. 2017. GCN5L1 modulates cross-talk between mitochondria and cell signaling to regulate FoxO1 stability and gluconeogenesis. *Nat Commun* 8: 523.
29. Moosbrugger-Martinz, V., M. Schmuth, and S. Dubrac. 2017. A Mouse Model for Atopic Dermatitis Using Topical Application of Vitamin D3 or of Its Analog MC903. *Methods Mol Biol* 1559: 91-106.
30. Das, J., C. H. Chen, L. Yang, L. Cohn, P. Ray, and A. Ray. 2001. A critical role for NF-kappa B in GATA3 expression and TH2 differentiation in allergic airway inflammation. *Nat Immunol* 2: 45-50.
31. Schindelin, J., I. Arganda-Carreras, E. Frise, V. Kaynig, M. Longair, T. Pietzsch, S. Preibisch, C. Rueden, S. Saalfeld, B. Schmid, J. Y. Tinevez, D. J. White, V. Hartenstein, K. Eliceiri, P. Tomancak, and A. Cardona. 2012. Fiji: an open-source platform for biological-image analysis. *Nat Methods* 9: 676-682.

32. Meitei, H. T., and G. Lal. 2023. T cell receptor signaling in the differentiation and plasticity of CD4(+) T cells. *Cytokine Growth Factor Rev* 69: 14-27.
33. Imanishi, T., C. Ishihara, S. Badr Mel, A. Hashimoto-Tane, Y. Kimura, T. Kawai, O. Takeuchi, K. J. Ishii, S. Taniguchi, T. Noda, H. Hirano, F. Brombacher, G. N. Barber, S. Akira, and T. Saito. 2014. Nucleic acid sensing by T cells initiates Th2 cell differentiation. *Nat Commun* 5: 3566.
34. Aarreberg, L. D., K. Esser-Nobis, C. Driscoll, A. Shuvarikov, J. A. Roby, and M. Gale, Jr. 2019. Interleukin-1beta Induces mtDNA Release to Activate Innate Immune Signaling via cGAS-STING. *Mol Cell* 74: 801-815 e806.
35. Liu, X., X. Cen, R. Wu, Z. Chen, Y. Xie, F. Wang, B. Shan, L. Zeng, J. Zhou, B. Xie, Y. Cai, J. Huang, Y. Liang, Y. Wu, C. Zhang, D. Wang, and H. Xia. 2023. ARIH1 activates STING-mediated T-cell activation and sensitizes tumors to immune checkpoint blockade. *Nat Commun* 14: 4066.
36. Hu, Z., F. Zhang, M. Brenner, A. Jacob, and P. Wang. 2023. The protective effect of H151, a novel STING inhibitor, in renal ischemia-reperfusion-induced acute kidney injury. *Am J Physiol Renal Physiol* 324: F558-F567.
37. Cohn, L., C. Herrick, N. Niu, R. Homer, and K. Bottomly. 2001. IL-4 promotes airway eosinophilia by suppressing IFN-gamma production: defining a novel role for IFN-gamma in the regulation of allergic airway inflammation. *J Immunol* 166: 2760-2767.
38. Lood, C., L. P. Blanco, M. M. Purmalek, C. Carmona-Rivera, S. S. De Ravin, C. K. Smith, H. L. Malech, J. A. Ledbetter, K. B. Elkon, and M. J. Kaplan. 2016. Neutrophil extracellular traps enriched in oxidized mitochondrial DNA are interferogenic and contribute to lupus-like disease. *Nat Med* 22: 146-153.
39. Jin, J., Y. Mu, H. Zhang, I. Sturmlechner, C. Wang, R. R. Jadhav, Q. Xia, C. M. Weyand, and J. J. Goronzy. 2023. CISH impairs lysosomal function in activated T cells resulting in mitochondrial DNA release and inflammaging. *Nat Aging* 3: 600-616.
40. Benoit-Lizon, I., E. Jacquin, T. Rivera Vargas, C. Richard, A. Roussey, L. Dal Zuffo, T. Martin, A. Melis, D. Vinokurova, S. H. Shahoei, A. Baeza Garcia, C. Pignol, S. Giorgiutti, R. Carapito, R. Boidot, F. Vegran, R. A. Flavell, B. Ryffel, E. R. Nelson, P. Soulas-Sprauel, T. Lawrence, and L. Apetoh. 2022. CD4 T cell-intrinsic STING signaling controls the differentiation and effector functions of T(H)1 and T(H)9 cells. *J Immunother Cancer* 10.
41. Decout, A., J. D. Katz, S. Venkatraman, and A. Ablasser. 2021. The cGAS-STING pathway as a therapeutic target in inflammatory diseases. *Nat Rev Immunol* 21: 548-569.
42. Balka, K. R., C. Louis, T. L. Saunders, A. M. Smith, D. J. Calleja, D. B. D'Silva, F. Moghaddas, M. Tailler, K. E. Lawlor, Y. Zhan, C. J. Burns, I. P. Wicks, J. J. Miner, B. T. Kile, S. L. Masters, and D. De Nardo. 2020. TBK1 and IKKepsilon Act Redundantly to Mediate STING-Induced NF-kappaB Responses in Myeloid Cells. *Cell Rep* 31: 107492.
43. Prabakaran, T., C. Bodda, C. Krapp, B. C. Zhang, M. H. Christensen, C. Sun, L. Reinert, Y. Cai, S. B. Jensen, M. K. Skouboe, J. R. Nyengaard, C. B. Thompson, R. J. Lebbink, G. C. Sen, G. van Loo, R. Nielsen, M. Komatsu, L. N. Nejsum, M. R. Jakobsen, M. Gyrd-Hansen, and S. R. Paludan. 2018. Attenuation of cGAS-STING signaling is mediated by a p62/SQSTM1-dependent autophagy pathway activated by TBK1. *EMBO J* 37.
44. Yu, J., X. Zhou, M. Chang, M. Nakaya, J. H. Chang, Y. Xiao, J. W. Lindsey, S. Dorta-Estremera, W. Cao, A. Zal, T. Zal, and S. C. Sun. 2015. Regulation of T-cell activation and migration by the kinase TBK1 during neuroinflammation. *Nat Commun* 6: 6074.
45. Bertoli-Avella, A. M., K. K. Kandaswamy, S. Khan, N. Ordonez-Herrera, K. Tripolszki, C. Beetz, M. E. Rocha, A. Urzi, R. Hotakainen, A. Leubauer, R. Al-Ali, V. Karageorgou, O. Moldovan, P. Dias, A. Alhashem, B. Tabarki, M. A. Albalwi, A. F. Alswaid, Z. N. Al-Hassnan, M. A. Alghamdi, Z. Hadipour, F. Hadipour, N. Al Hashmi, L. Al-Gazali, H. Cheema, M. S. Zaki, I. Huning, A. Alfares, W. Eyaid, F. Al Mutairi, M. Alfadhel, F. S. Alkuraya, N. A. Al-Sannaa, A. M. AlShamsi, N. Ameziane, A. Rolfs, and P. Bauer. 2021. Combining exome/genome sequencing with data repository analysis reveals novel gene-disease associations for a wide range of genetic disorders. *Genet Med* 23: 1551-1568.

602 46. Powers, J. M., Y. Liu, A. B. Moser, and H. W. Moser. 1992. The inflammatory myelinopathy of
603 adreno-leukodystrophy: cells, effector molecules, and pathogenetic implications. *J*
604 *Neuropathol Exp Neurol* 51: 630-643.
605 47. Lochner, M., L. Berod, and T. Sparwasser. 2015. Fatty acid metabolism in the regulation of T
606 cell function. *Trends Immunol* 36: 81-91.
607 48. Malik, K., H. He, T. N. Huynh, G. Tran, K. Mueller, K. Doytcheva, Y. Renert-Yuval, T. Czarnowicki,
608 S. Magidi, M. Chou, Y. D. Estrada, H. C. Wen, X. Peng, H. Xu, X. Zheng, J. G. Krueger, A. S. Paller,
609 and E. Guttman-Yassky. 2019. Ichthyosis molecular fingerprinting shows profound T(H)17
610 skewing and a unique barrier genomic signature. *J Allergy Clin Immunol* 143: 604-618.
611 49. Wu, K., A. Takanohashi, S. Woidill, A. Seylani, G. Helman, P. Dias, J. Beers, Y. Lin, C. Simons, E.
612 Wolvetang, J. Zou, A. Vanderver, and M. N. Sack. 2022. Generation of human induced
613 pluripotential stem cells from individuals with complex heterozygous, isogenic corrected, and
614 homozygous Bloc1s1 mutations. *Stem Cell Res* 64: 102905.

615

616

Figures and Figure Legends:

Figure 1

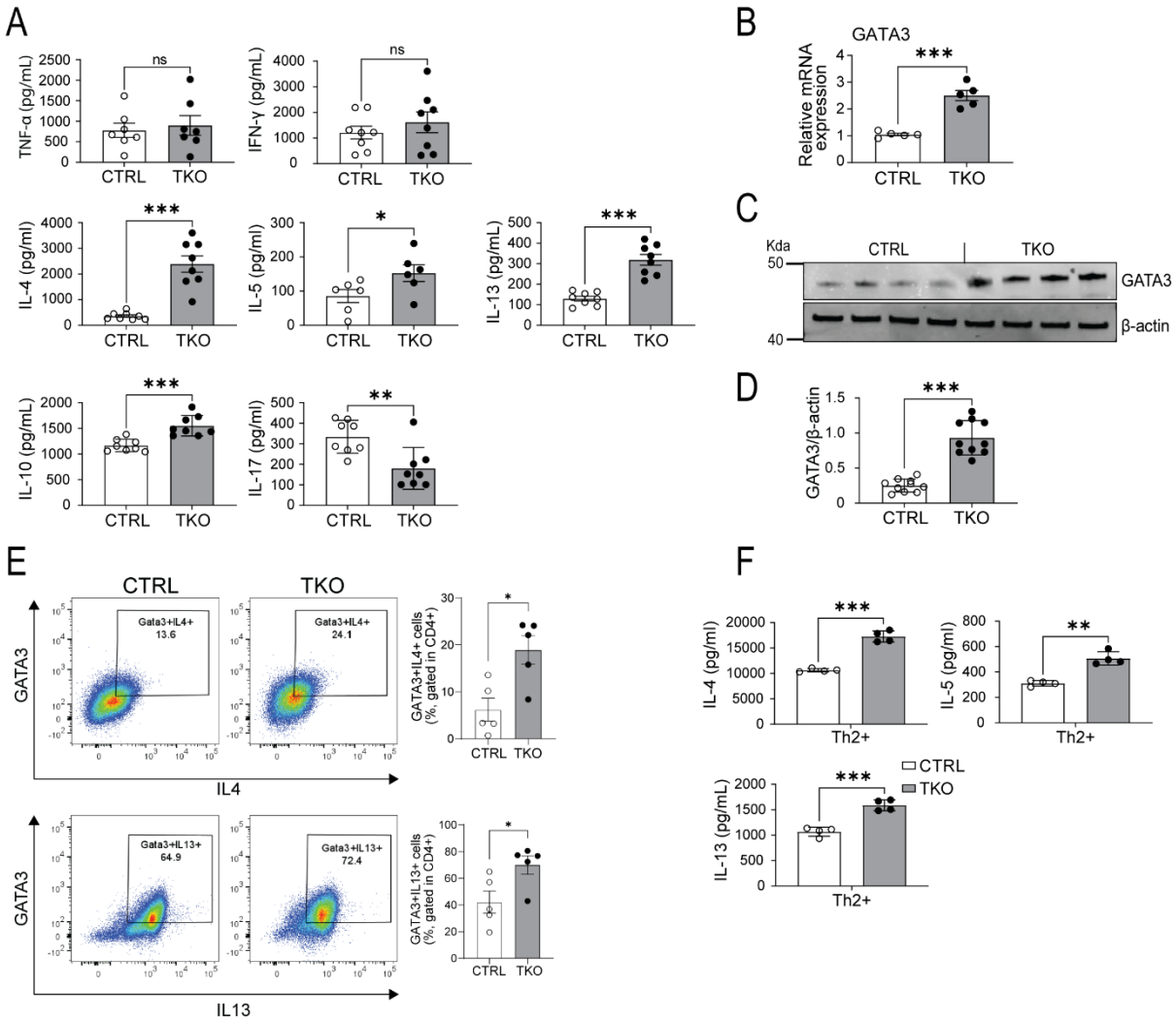

Figure 1. BLOC1S1 depleted CD4⁺ preferentially augments T_H2 immune responsiveness

(A) T_H1, T_H2, Treg and T_H17 associated cytokines released from $CD4^+$ T cells isolated from the spleen of control (CTRL) and TKO mice, activated with antibodies directed against CD3 and CD28 for 3 days (n=7-8 per group). **(B)** qRT-PCR showing relative mRNA expression levels of GATA3 (n=5 per group). **(C)** Representative immunoblot analysis of GATA3 and β-actin. **(D)** Densitometry analysis of the relative protein levels of GATA3/β-actin in $CD4^+$ T cell lysate from spleen of control and TKO mice (n=10 per group). **(E)** Representative flow-cytometric analysis of intracellular cytokines $GATA3^+IL4^+$ and $GATA3^+IL13^+$ in $CD4^+$ T cells (n=5 per group). Values represent mean ± SEM.. **(F)** IL-4, IL-5 and IL-13 cytokine release in $CD4^+$ isolated from the spleen of control and TKO mice, activated with αCD3 and αCD28, supplemented with T_H2 differentiation cocktail for 3-4 days (n=4 per group). Values represent mean ± SEM. *P<0.05, *p<0.05, **p<0.01, ***p<0.001 vs. control mice using unpaired two-tailed student-t-test. FSC, forward scatter; SSC, side scatter.

Figure 2

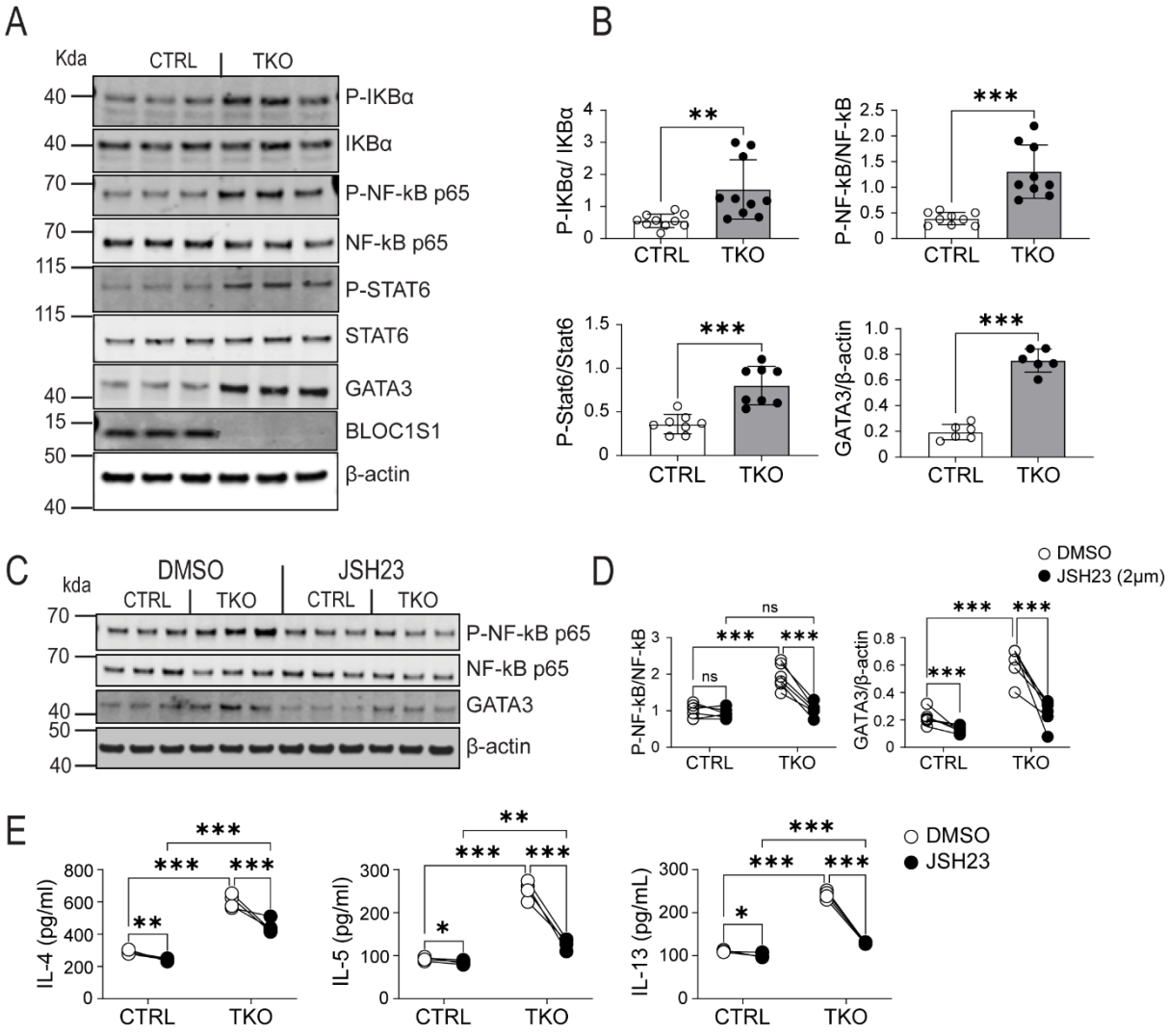

Figure 2. BLOC1S1 deficiency results in enhanced IKK, NF-kB and STAT6 phosphorylation and GATA3 activity.

(A) Representative immunoblot for phospho-IκBα , IκBα, phospho-NF-κB p65, NF-κB p65, phospho-STAT6, STAT6, GATA3, BLOC1S1 and β-actin from splenic CD4⁺ T cells lysates from control and TKO mice. **(B)** Quantitation of the ratio of P-IκBα/IκBα, P-NF-κB p65/NF-κB p65, P-STAT6/STAT6 and GATA3/β-actin by densitometry analysis (n=6-10). **(C)** Representative immunoblot analysis of P-NF-κB P65, NF-κB p65, GATA3 and β-actin from contron and TKO CD4⁺ T cells incubated with either DMSO or 2 μM JSH23 for 12 hours. **(D)** Quantitation of the ratio of P-NF-κB p65/NF-κB p65 and GATA3/β-actin by densitometry analysis (n=5-6). **(E)** IL-4, IL-5 and IL-13 cytokine release in activated CD4⁺ T cells incubated with DMSO or JSH23 2uM for 12 hours (n=5-6). Values represent mean ± SEM. *p<0.05, **p<0.01, ***p<0.001 vs control mice by two-way ANOVA followed by the Tukey's post hoc test or unpaired two-tailed student-t-test.

649

Figure 3

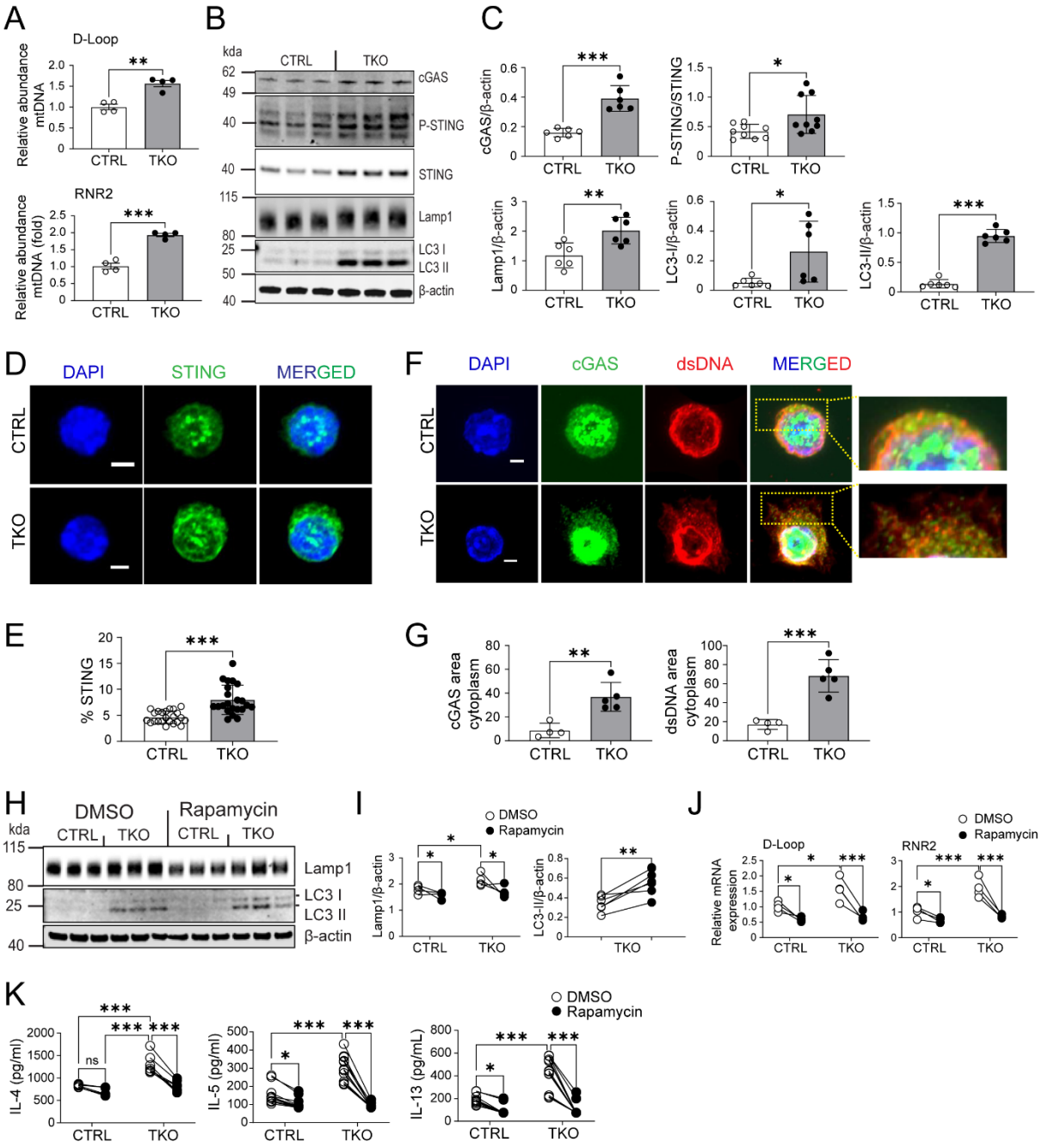

650

651

652 **Figure 3. BLOC1S1 deficiency results in mtDNA release into cytosol and activation of cGAS-**
653 **STING pathway.**

654 **(A)** qRT-PCR showing relative mRNA expression levels of D-Loop and RNR2 in $CD4^+$ T cells (n=4).
655 **(B)** Representative immunoblot of cGAS, P-STING, STING, Lamp1, LC3 I/II and β-actin from CTRL
656 and TKO $CD4^+$ T cells. **(C)** Protein quantitation and ratio of cGAS/β-actin, P-STING/STING, Lamp1/β-
657 actin, LC3 I/β-actin, LC3 II/β-actin and GATA3/β-actin by densitometry analysis (n=6-9). **(D)**
658 Representative fluorescence images of STING (green) in activated $CD4^+$ T cells. Nuclei were
659 counterstained with 4',6-diamidino-2-phenylinodole (DAPI) ((blue). Scale bar = 2 μm. **(E)**
660 Semiquantitative analysis of the mean intensity (%) of STING staining from CTRL and TKO $CD4^+$ T

cells (n=7 per group). **(F)** Representative fluorescence images of cGAS (green) and dsDNA (red) in activated $CD4^+$ T cells. Nuclei were counterstained with DAPI (blue). Scale bar 2 μm. **(G)** Semiquantitave analysis of the Fluorescence area of cGAS and dsDNA staining in the cytoplasm (n=4-5 per group). **(H)** Representative immunblots for Lamp1, LC3I/II and β-actin from CTRL and TKO $CD4^+$ T cells in response to either DMSO or 100 nM Rapamycin for 48 hours. **(I)** Protein densitometry ratio of Lamp1/β-actin and LC3-II/β-actin by densitometry analysis (n=5 per group). **(J)** qRT-PCR showing relative mRNA expression levels of D-Loop and RNR2 from CTRL and TKO $CD4^+$ T cells following DMSO or Rapamycin 100nm incubation for 48 hours. **(K)** IL-4, IL-5 and IL-13 cytokine release in activated $CD4^+$ T cells following DMSO or Rapamycin 100nM incubation (n=8-12 per group). Values represent mean ± SEM. *p<0.05, **p<0.01, ***p<0.001 vs control mice by two-way ANOVA followed by the Tukey's post hoc test or unpaired two-tailed student-t-test.

Figure 4

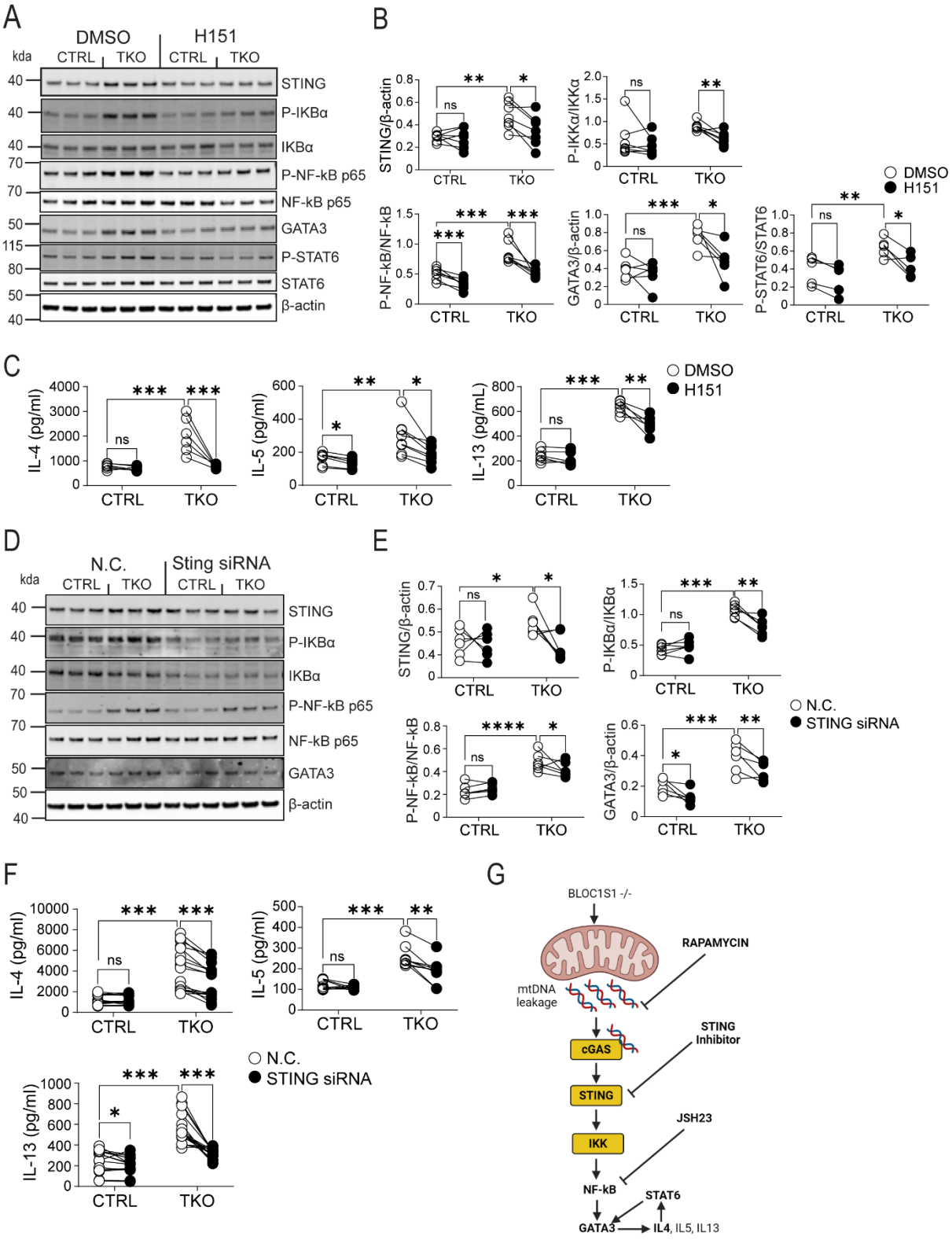

Figure 4. STING knockdown resulted in reduced T_H2 cytokines in BLOC1S1-/- CD4⁺ T cells.

(A) Representative immunoblots for STING, P-IκBα, IκBα, P-NF-κB p65, NF-κB p65, GATA3, P-STAT6, STAT6 and β-actin from CTRL and TKO CD4⁺ T cells following DMSO or H151 (500 nM) incubation for 48 hours. **(B)** Protein quantitation and ratio of STING/β-actin, P-IKBα/IKBα, P-NF-kB

689 P65/NF-kB P65, GATA3/β-actin and P-STAT6/STAT6 by densitometry analysis (n=6-7 per group). **(C)**
690 IL-4, IL-5 and IL-13 cytokine release in activated $CD4^+$ T cells treated with either DMSO or H151
691 (500nM) (n=6-7 per group). **(D)** Representative immunoblots for STING, P-IκBα, IκBα, P-NF-κB p65,
692 NF-kB p65, GATA3 and β-actin from CTRL and TKO $CD4^+$ T cells incubated with negative control
693 (N.C.) or with STING siRNA. **(E)** Protein quantitation and ratio of STING/β-actin, P-IκBα/IκBα, P-NF-
694 κB P65/NF-κB P65 and GATA3/β-actin by densitometry analysis (n=6 per group). **(F)** IL-4, IL-5 and
695 IL-13 cytokine release in activated $CD4^+$ T cells incubated with either N.C. or STING siRNA (n=9-18
696 per group). **(G)** Schematic representation of proposed mechanistic pathway. Values represent mean
697 ± SEM. *p<0.05, **p<0.01, ***p<0.001 vs control mice by two-way ANOVA followed by the Tukey's
698 post hoc test or unpaired two-tailed student-t-test.

699

700

701

702

703

704

705

Figure 5

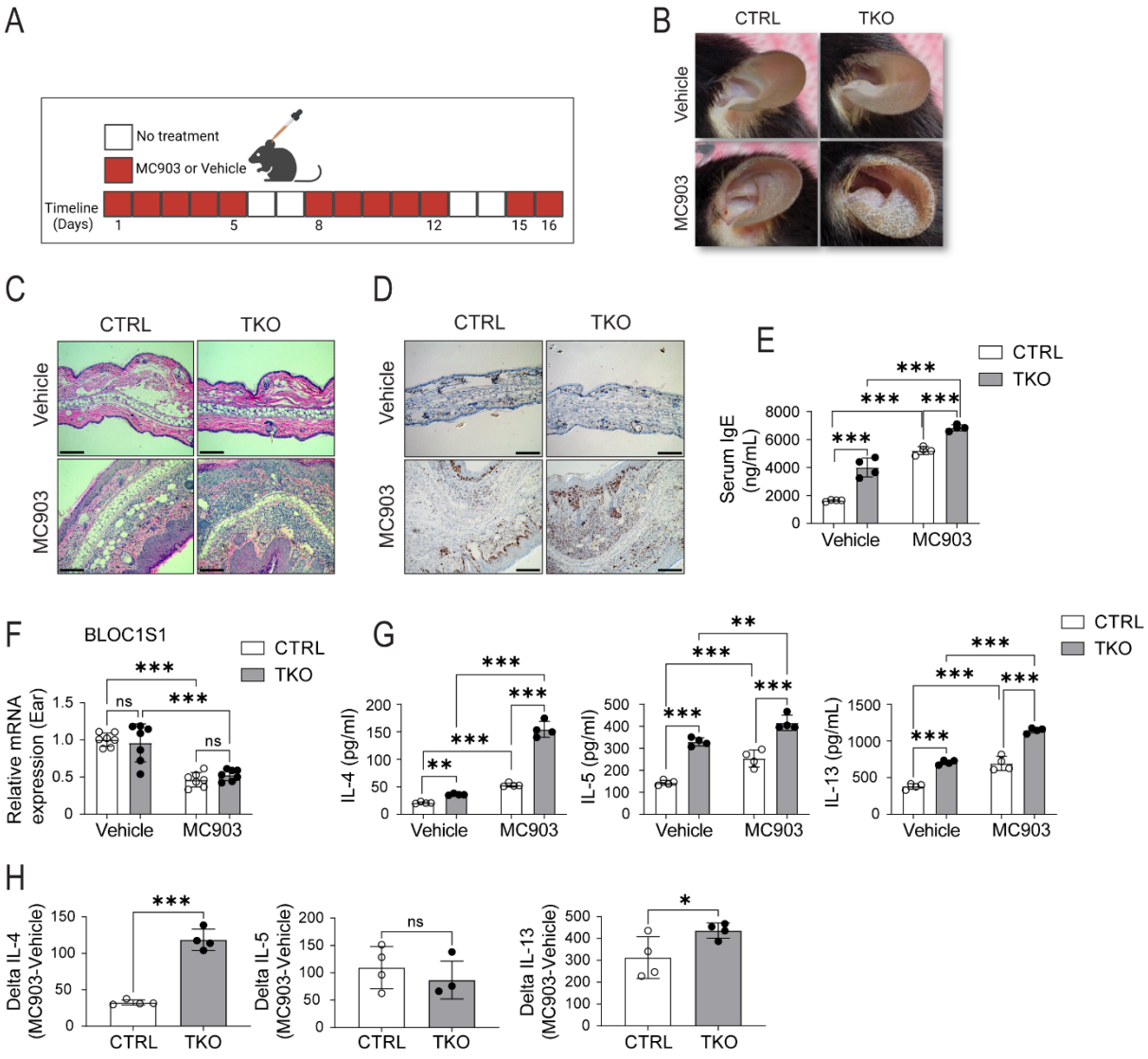

Figure 5. Increased calcipotriol (MC903) induced atopic dermatitis in TKO mice.

(A) Daily study protocol for MC903 induced dermatitis (in red). **(B)** Gross appearance of Ethanol or MC903 application to CTRL and TKO mouse ears at day 12. **(C)** Representative H&E staining of ear sections at day 12. Scale bar = 100um. **(D)** Representative Ki67 staining of ear sections at day 12. Scale bar = 100um. **(E)** Plasma IgE levels from the mice following the topical application of ethanol or MC903 (n=4 per group). **(F)** qRT-PCR showing relative mRNA expression levels of BLOC1S1 from mourse ears in response to ethanol or MC903 (n=7 per group). **(G)** IL-4, IL-5 and IL-13 cytokine secreted levels at day 12 from CTRL and TKO $CD4^+$ T cells isolated from auricular lymph nodes following ethanol or MC903 topical application (n=4 per group). **(H)** Delta IL-4, Delta IL-5 and Delta IL-13 cytokine values of CTRL and TKO $CD4^+$ T cells in response to MC903 (n=4 per group). Values represent mean ± SEM. *p<0.05, **p<0.01, ***p<0.001 vs control mice by two-way ANOVA followed by the Tukey's post hoc test or unpaired two-tailed student-t-test.

Figure 6

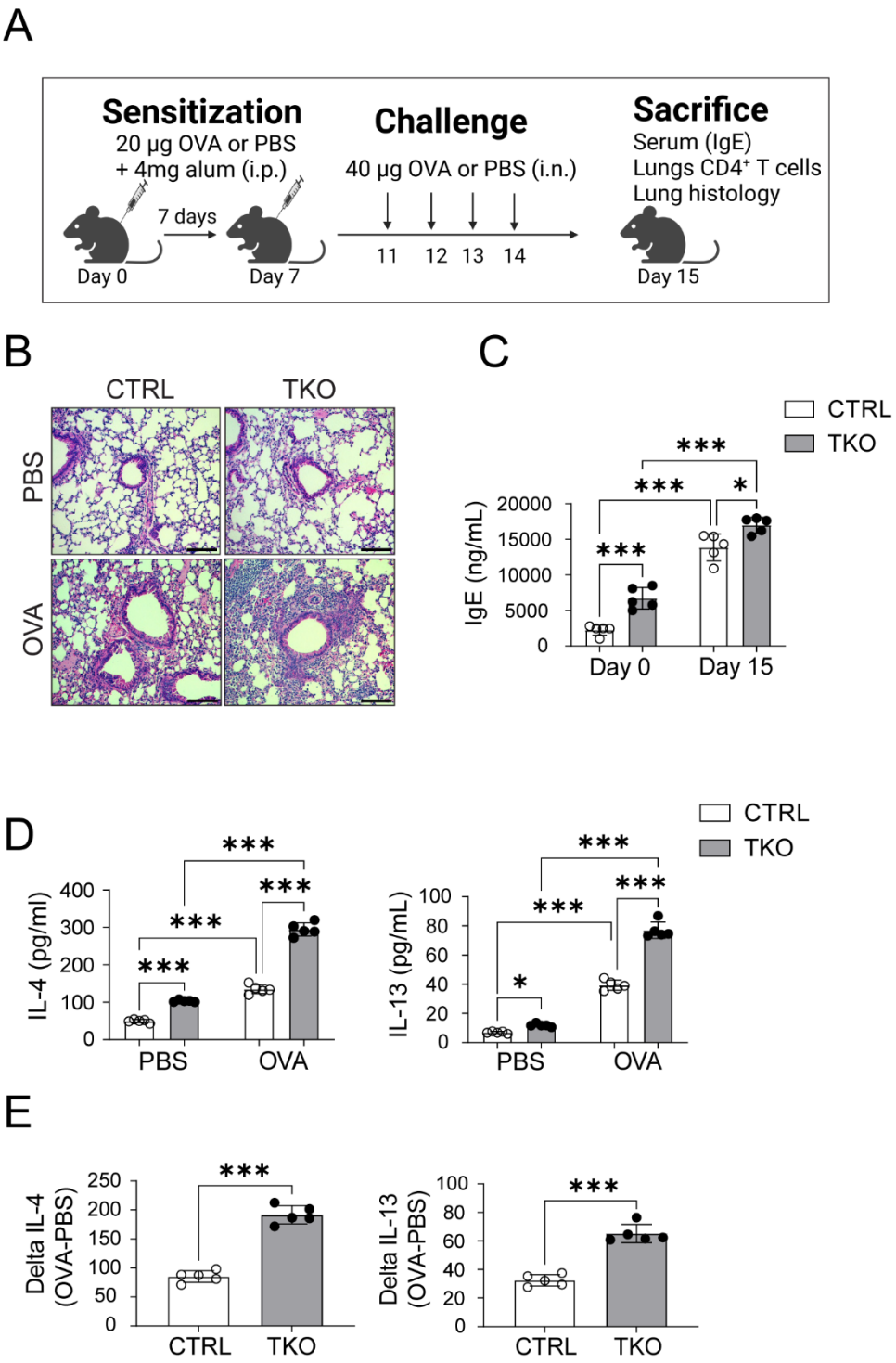

Figure 6. Increased ovalbumin induced airway inflammation in TKO mice.

(A) Daily protocol for ovalbumin induced airway inflammation in mice. **(B)** Representative H&E staining of lungs of PBS and Ovalbumin (OVA) administered CTRL and TKO mice. Scale bar = 100um. **(C)** Plasma IgE from the CTRL and TKO mice following PBS or OVA administration (n=5 per

730 group). **(D)** IL-4 and IL-13 cytokine release from $CD4^+$ T cells isolated from the lungs of CTRL and
731 TKO mice in response to PBS or OVA administration (n=5 per group). **(E)** Delta IL-4 and Delta IL-5
732 levels (n=5 per group). Values represent mean ± SEM. *p<0.05, **p<0.01, ***p<0.001 vs control mice
733 by two-way ANOVA followed by the Tukey's post hoc test or unpaired two-tailed student-t-test.

734

735